Research Square

Preprints are preliminary reports that have not undergone peer review.
They should not be considered conclusive, used to inform clinical practice,
or referenced by the media as validated information.

Study of Thermal and Hydrodynamic Behavior of Incone-625 Additively Manufactured Surfaces with Varying Scan Orientations: Surface Topography Analysis, Experimental Investigation with Reproducibility Tests and CFD Verification

Kuldeep Mandloi

kuldeep.mandloi03@gmail.com

University of North Carolina at Charlotte

Harish Cherukuri

University of North Carolina at Charlotte

Angela Allen

University of North Carolina at Charlotte

Jimmie Miller

University of North Carolina at Charlotte

Research Article

Keywords: Surface topography, additive manufacturing, scan orientations, Heat-transfer, fluid-flow, experiments, CFD, sand-grain roughness

Posted Date: September 1st, 2026

DOI: https://doi.org/10.21203/rs.3.rs-10670661/v1

License: This work is licensed under a Creative Commons Attribution 4.0 International License.
Read Full License

Additional Declarations: No competing interests reported.

Study of Thermal and Hydrodynamic Behavior of Incone-625 Additively Manufactured Surfaces with Varying Scan Orientations: Surface Topography Analysis, Experimental Investigation with Reproducibility Tests and CFD Verification.

Abstract

Additive manufacturing (AM), particularly laser powder bed fusion (LPBF), is of great interest to many industries such as tool and die making, IC manufacturing, medical implants, electronic cooling, and aerospace communities as it can be used to manufacture parts with complex internal and external geometries. This is in contrast to conventional manufacturing methods that limit the complexity of part designs. Particularly, the interests are the manufacturing of parts with cooling channels consisting of complex surface topographies designed to improve thermal performance of the cooling channels. Additive manufacturing offers an alternative that has the potential to overcome this limitation. For a successful industrial adoption of AM for parts requiring complex cooling channels, an understanding of the relationship between the as-built surface finish and heat transfer is needed. In LPBF, there are numerous build parameters, such as scan orientation during the build, which affect the final part surface topography and hence heat transfer. The primary focus of this work is to study the effects of AM roughness characteristics on heat transfer from the corresponding AM surfaces and pressure drop across cooling channels. Both numerical and experimental investigations are carried out for this purpose. Computational Fluid Dynamics (CFD) models for mini-channels using StarCCM+ (a commercial CFD code) were developed by acquiring the roughness data from real AM surfaces with various roughness parameters. To explore the correlation between sand-grain modeled roughness and AM surface roughness with 90° build orientation, CFD simulations for the entire system model (experimental setup) were employed. Based on CFD findings, an exchangeable experimental setup was developed and on the basis of roughness characterizations, the AM parts with three critical orientations (0°, 45°, and 90°) were fabricated and then machined to the required shape and size to fit into the set-up. In addition, an Inconel part with a smooth surface has been machined from a forged Inconel-625 circular bar to serve as the baseline control condition. Both CFD and experimental results were compared for different Reynolds numbers, and the experimental results validated the CFD findings. Significant differences in the Nusselt numbers and pressure drops were observed across the different AM surfaces, with the surface with 90° build orientation performing best in terms of heat transfer for a given build conditions.

Keywords: Surface topography, additive manufacturing, scan orientations, Heat-transfer, fluid-flow, experiments, CFD, sand-grain roughness

1. Introduction

The use of additive manufacturing (AM) is growing, particularly where complex cooling systems are required, for example in gas turbine engines. It is necessary to explore the relationship between the topography of AM surfaces with different scan orientations and their effects on heat transfer. Laser powder bed fusion (LPBF) is one of the most common AM techniques in which a laser beam is used to melt thin layers of metal powder. Once the layer gets solidified, another powder layer is spread using a spreader and the same process repeats till the part is complete. In LPBF, the surface topography of the final product is greatly affected by the build parameters such as laser scanning speed, type of material, laser power and part orientation [1]. Many researchers have investigated the effects of scan orientations on surface topography of AM parts. Fox et al. [2] fabricated AM surfaces using LPBF. They varied the build orientation of the surfaces to the Z-axis of the build chamber and position within the chamber and then analyzed the relationship between build orientation and surface. In addition, Delgado et al [3] also showed that the build angles greatly affect the roughness characteristics of AM surfaces. However, this research was limited to two scan orientations only. Some other studies were also carried out to investigate the effects of AM surface roughness on heat-transfer and fluid flow. Kandlikar et al [5] fabricated the micro-channels and studied the effect

of surface roughness on pressure drop. They corelated the maximum profile peak height and spacing between profile elements with friction factor. Snyder et al [4] built microchannel test coupons with different build angles and investigated the effects of AM surface roughness on heat-transfer and pressure drop. In addition, some other researchers also investigated the effects of surface roughness of AM parts on heat-transfer and worked on quantifying the performance of AM surfaces in terms of heat-transfer and friction factor [6]. However, most of these studies were limited to channel geometries only and a detailed investigation on the effects of built orientation (including the effects of overlapping weld-tracked orientation, ejecta from the melt pool, partially melted powder particles and waviness) on heat transfer and fluid flow characteristics were not explored. In addition, Kuldeep et al. [1,7] investigated the effects of AM build orientation on heat-transfer by physically modeling the AM surfaces. In that study, they used AM surfaces with different scan orientations and then carried out surface measurement of those surfaces. From the surface measurement data, they created simplified AM surfaces for carrying out CFD investigation and found that the surface with 90° angle to fluid flow is most effective surface in terms of heat-transfer but also gave highest pressure drop for different flow conditions. The current study is the extension of this one with experimental investigation.

There is a long history of studies on the effects of surface topography on heat transfer. The most widely used resource for roughness data made available by Moody (1994). Moody's chart is based on the friction factor calculated using the Darcy-Weisbach equation and it also corelates with experimental data from Nikuradse (1993). Nikuradse coated an internal pipe surface with a layer of sand grains using glue and then performed various experiments and measured pressure drop and friction factor [11]. He defined the roughness height as the average diameter of sand-grain and corelated his experiments accordingly. Though, the actual rough surfaces specifically the AM surfaces do not represent such monolayer of sand-grains [12] rather it is a combination of different surface topographic features such as stepovers, presence of particles, peaks and valleys of different heights and shapes [13]. To overcome these limitations, an equivalent sad-grain roughness model was recommended where sand grain size can be expressed in a dimensionless form using dynamic viscosity (μ) and the friction velocity u*. In most of the literature, sand-grain roughness k_s was reported based on several experimental data from turbulent flow in fully rough regimes. Many of such studies suggested to use R_a as a parameter to define Ks, such as Foster et al. [15] used $k_s/R_a = 2$ for ground surfaces and for a sandpaper $k_s/R_a = 7$ for a different grit sizes. However, R_a is not able to describe the effect of areal topography on fluid flow and heat transfer. Also, Bogard et al. [14] found that using R_a as a single parameter to define the equivalent roughness is not sufficient to incorporate most of the critical surface topographic features. Therefore, later many authors defined the sand-grain size based on other important surface features such as probability density function (PDF), waviness, roughness slope [13] and consequently Musker [16] used S_q to define the sand-grain roughness. However, he also modified the K_s in terms of average roughness slope s_p, skewness s_k, and kurtosis k_u which account for most of the realistic surface features. Therefore, in current study for roughness modeling using sand-grain roughness model, S_q is used as a parameter to define sand-grain roughness size. However, the current study is an extension of the study carried out by same authors in [1,7]. In this study, based on the results of [7], the AM surfaces with three critical scan orientations (0°, 45°, and 90°) were fabricated. In addition, an Inconel part with a smooth surface with $S_q = 5.03$ μm (Filter: low pass 100 μm FFT, form removal: cylinder, Area: 4X20 mm and objective: 20X) has been machined from a forged Inconel-625 circular bar to serve as the baseline control condition. Also, one of the most important novelty of this research was to design and develop an exchangeable experimental set-up to quantify the effects of scan orientation on heat-transfer and pressure drop for various flow conditions and also to validate CFD results. The effects of AM surface roughness on heat-transfer and fluid-flow were analyzed in terms of Nusselt Number, pressure drop and friction factor.

2. Nomenclature

ρ	Density of fluid (kg/m^3).
A_c	Cross sectional area of the channel (mm^2)
A_s	Surface area (mm^2)
B	Channel width (mm)
D_H	Mean hydraulic diameter (mm)
F	Friction factor.
H	Heat transfer coefficient (w/m^2-K)
I	Current (Amp)
K_f	Thermal conductivity of water (w/m-K)
L_{ch}	Channel length (mm)
L_O	Overall length (mm)
Nu	Average Nusselt number.
Ω	Ohm
q	Heat input (w)
q"	Heat flux (w/m^2)
R	Resistance (Ω)
Re	Reynolds number
STD	Standard Deviation
T_m	Bulk mean temperature (c)
T_s	Interface surface temperature (c)
T_{out}	Surface average outlet temperature (c)
μ	Dynamic viscosity (N-m/s)
v	Mean velocity (m/s).
u*	Friction velocity (m/s)
V	Voltage (volt)
ΔP	Pressure drop (kPa)
ω	Turbulent frequency
EXP	Experimental
CFD	Computational fluid dynamics
CSI	Coherence scanning interferometry
RMS	Root mean square
R_a	Mean of roughness height
S_q	RMS of roughness heights
R_z	Distance from peak to valley
k_s	Sand-grain roughness height
s_p	roughness slope
s_k	skewness
k_u	kurtosis
sg	Sand-grain

3. Fabrication of AM surfaces

AM surfaces with three different scan orientations (0^0, 45^0 and 90^0) were fabricated at NIST facility using Laser powder bed fusion (LPBF) process. on an EOS M290 machine using nominal parameters recommended by the machine manufacturer and summarized in Table 1 (from "Surface topography process signatures in nickel superalloy 625 additive manufacturing"

Table: 1 Nominal build conditions

Laser power	285 W
Velocity	960 mm/s
Powder	EOS IN625; D50 = 27.1 μm
Layer thickness	40 μm nominal
Step over	110 μm
Stripe width	10 mm

For reproducibility and repeatability tests, three samples for each orientation were printed. Fig. 1 shows the printed AM parts with different scan orientations.

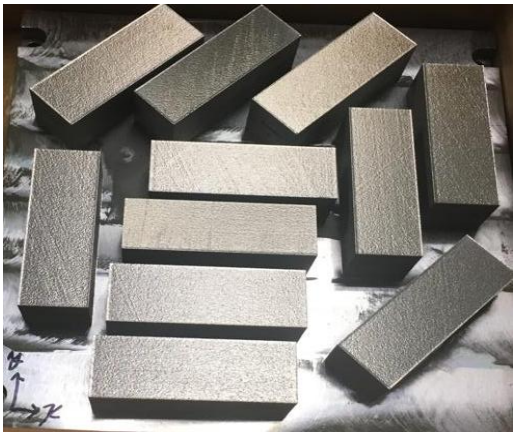


Fig. 1 Fabricated AM parts with different scan orientations.

4. Fabrication of resin part using SLA

To provide insulation from the side and upper walls and to reduce heat leak to environment, one half of the section of experimental setup was printed using Stereolithography (SLA) technique and the material used was Formlab high temperature resin. In this process, parts were printed using Formlab SLA 3-D printer. Fig. 2 depicts the entire process from printing to after wash and final product.



Fig. 2 3-D printing of resin part through SLA technique.

5. Surface roughness characterization

To explore the roughness characteristics of AM surfaces with different orientations, surface roughness characterization was carried out using Zygo ZeGage™ Pro HR coherence scanning interferometer (CSI) with a 5.5X objective (NA: 0.15). The areal measurements were taken from the mid-section of 20X4 mm (shown in Fig. 3) of each AM surface. For the areal measurement, stitching (adoptive setting) was used and based on field of view (3.02) of the object and area (20X4 mm) to be measured, a stitch (with 20% overlapping) of 2 rows and 9 columns was configured and the nominal scan length used was 500 µm with scan origin from top (upper limit). To analyze surface characteristics of these surfaces, low pass Fourier filter (100 um) was used, and cylindrical form was removed. and Fig. 4 of represents the roughness heights of different surfaces in x and y directions

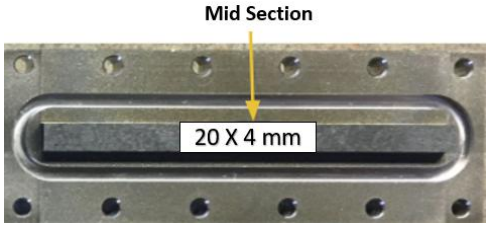


Fig. 3 Area measured using CSI

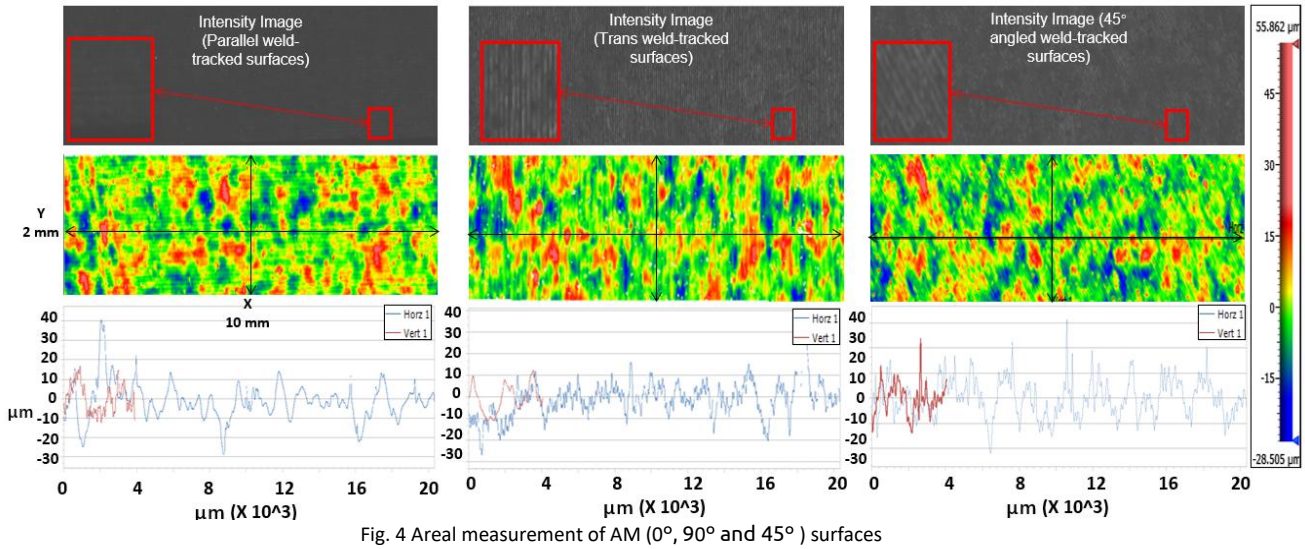
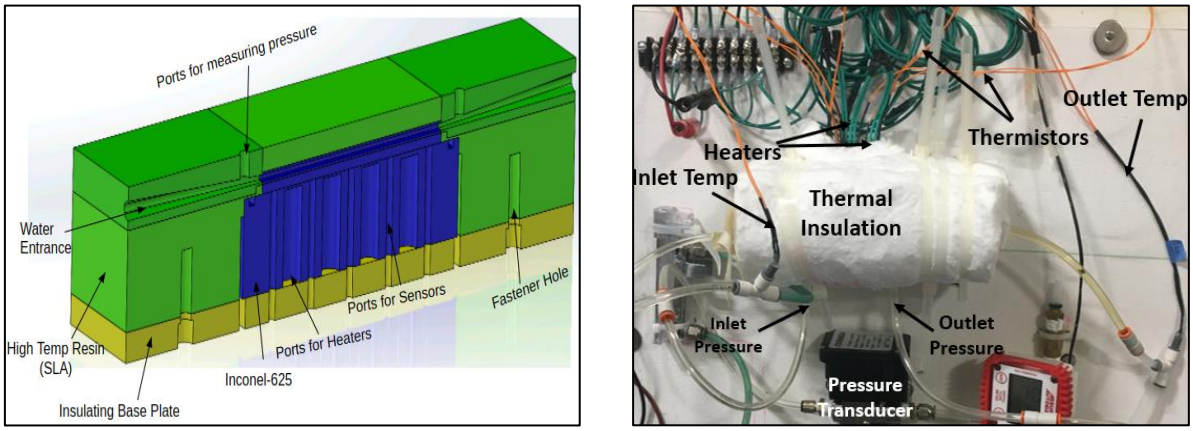


Fig. 4 Areal measurement of AM (0°, 90° and 45°) surfaces
(Filter: 100 µm low pass FFT, Form removal: Cylinder).

6. Experimental setup

To confine the effects of AM surfaces on heat-transfer and flow characteristics, the experimental setup was designed in a manner where the side and upper walls were assumed to be acting like insulating boundaries. The setup was designed and fabricated such that it can facilitate the exchange of AM parts for different experiments. Therefore, it was developed in two halves and then assembled (Fig. 5). One half of this setup is made of Formlab high-temp carbon resin [19] and was fabricated using stereolithography (SLA) and the other half of this setup is an exchangeable one and it is made of Inconel-625 using LPBF technique. The selection of fabrication techniques was based on material type and the complexity of the set-up. The entire assembly of the experimental setup has been discussed in section 6.2.



(a) (b)

Fig. 5 (a) Half-sectioned CAD model of set-up, (b) A real experimental set-up.

6.1 Sample preparation

AM samples were prepared by following the process depicted in Fig. 6 The process starts from printing AM surfaces with different scan orientations and after that they were removed from the build plate using wire-EDM. To relieve the residual stresses occurred during 3-D printing, the heat-treatment of these samples became necessary before machining. Heat-treatment was carried out by following the ISO 6892-1 B10 tensile test standards [18] and accordingly samples were kept at 900° C for four hours and then they were allowed to cool to the environmental temperature followed by machining to the required shape and size.

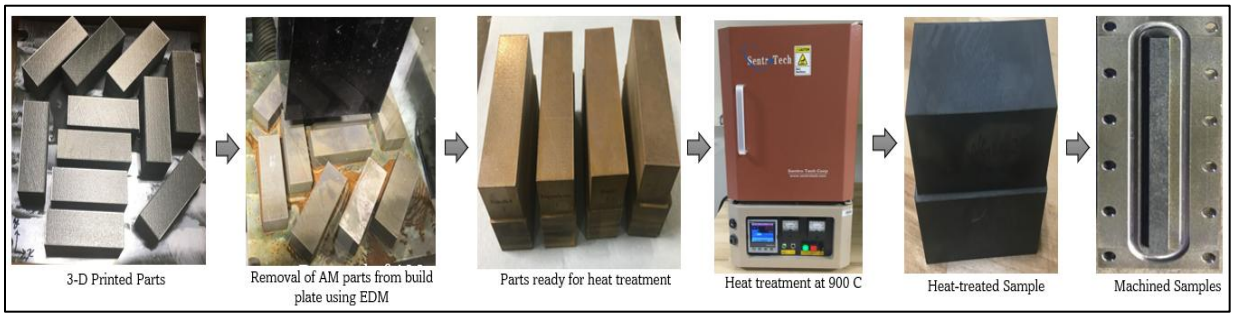


Fig. 6 Process followed during sample preparation

6.1.1 Heat treatment

To relieve residual stresses of AM samples (after printing) before machining, heat-treatment of each sample was carried out separately. For heat-treatment, AM samples were kept at 900^0 C for four hours and were allowed to cool in the oven for next six hours (Annealing was performed). To prevent the surface topography of AM samples from being changed due to oxidation, stainless steel wrapper

(shown in Fig. 7) was used to wrap these samples. To ensure consistency, surface measurements were taken before and after heat-treatment (shown in Fig. 8). For this measurement, the same instrument Zygo ZeGage™ Pro HR coherence scanning interferometer (CSI) was used with 20 X objective. Here the low-pass 100 um FFT filter was used along with removal of cylindrical form. The measurement area was 4X4 mm and the roughness heights with PSD were plotted along vertical to the lay. From roughness heights and PSD analysis, we did not find any significant difference in surface topography before and after heat-treatment and S_q values further confirm this statement.

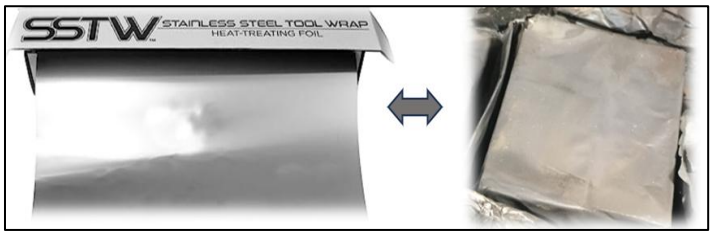
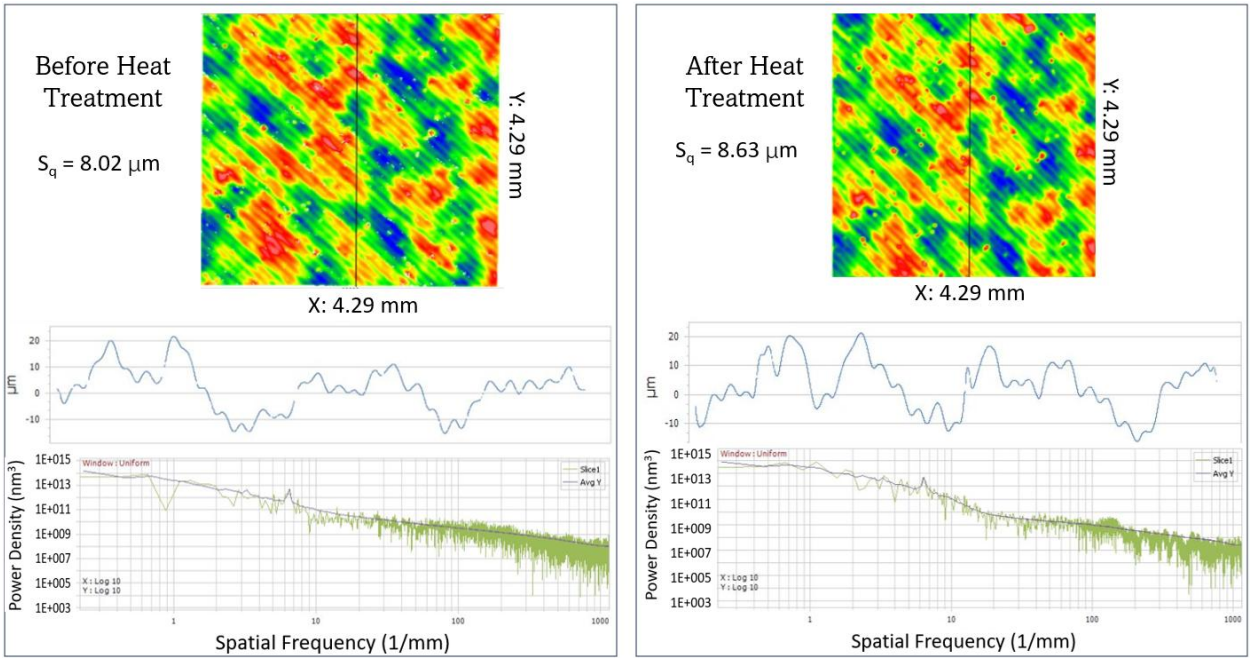


Fig. 7 Stainless-steel wrapper used to prevent oxidation during heat-treatment



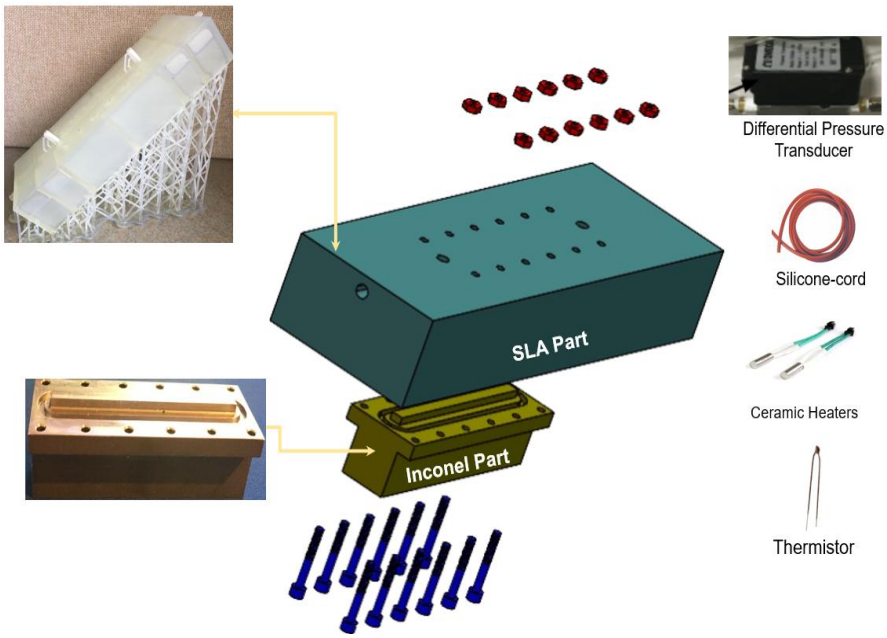
(a) (b)

Fig. 8 (a) CSI measurement Before heat-treatment, (b) CSI measurement after heat-treatment (Filter: Low pass FFT (100 um), Objective: 20 X)

6.2 Assembly

As discussed before, the experimental setup was made in two halves to make it an exchangeable set-up and then it was assembled. The setup was designed such that it can accommodate all the measuring devices along with cylindrical heaters for providing continuous heat supply. For smooth entry and to prevent back flow at the exit, converging-diverging sections were provided at the inlet and outlet, respectively. To provide constant heat input and to measure, temperature along the length of the channel, holes of varied sizes (according to the size of heaters and thermistors) with +0.01 mm tolerance limit were created to accommodate the cylindrical ceramic heaters and thermistors at the bottom of the AM parts. Two other holes of same size were created on the top of the SLA part (near inlet and outlet) for measuring the pressure drop across the channel. A digital pressure transducer was calibrated and used during all the experiments. Preventing the water leakage during experiments, O-ring grooves were made on each AM part and an O-ring seal was placed.

The detailed assembly of experimental set-up is shown in Fig. 9.



(a)

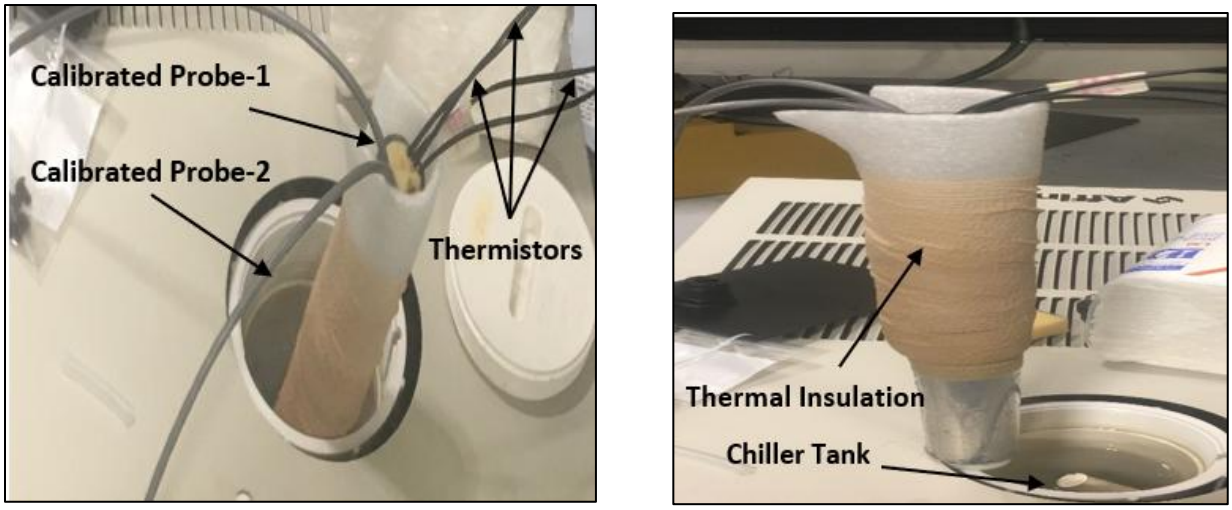


(b)

Fig. 9 (a) Detailed view of assembly, (b) Final assembly.

7. Calibration of thermistors

To measure the temperature at various locations during experiments, 5 KΩ thermistors were used after calibration. The thermistors were calibrated with the help of FLUKE CALIBRATION 3560: Extended Communications Module (temperature resolution: 0.001 °C, temperature stability: ±0.05 °C) using AS115-4WIRE thermistors (stability: 0.001 °C between 0 °C – 100 °C) . For the calibration, two calibrated temperature probes (with bias ± 0.05 °C up to 40 °C) along with four thermistors were placed inside the Al cylinder (3/4th insulated from the top) and later this cylinder was placed into the chiller tank (shown in Fig. 10) and measurements (till the thermistors reach steady-state) were taken for different chiller temperature at different time intervals.



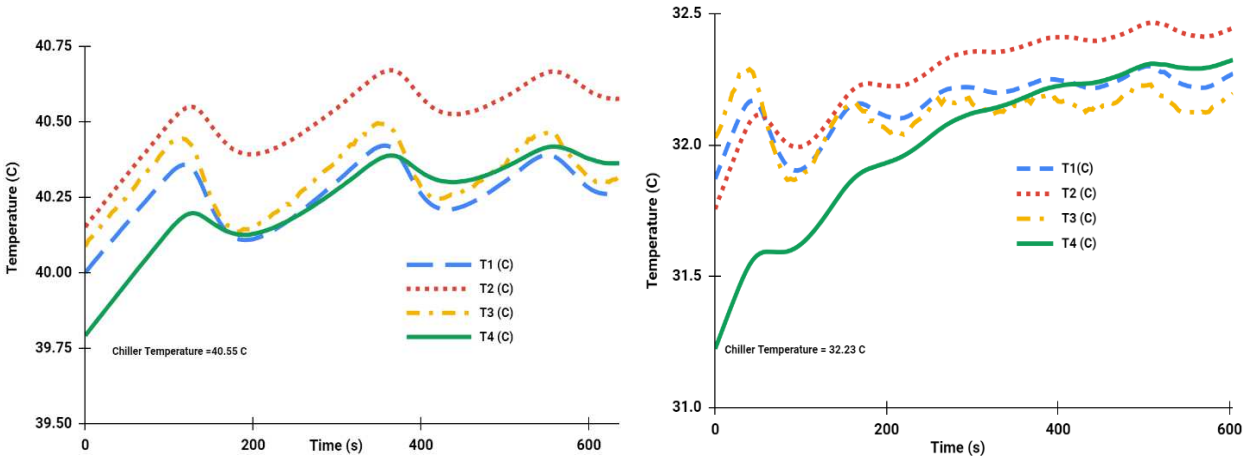
(a) (b)

Fig. 10 (a-b) Calibration set-up

Fig. 11 (a-b) shows the temperature data for two different chiller temperatures, and from these data it is noticeable that all the thermistors are calibrated with less than 1% uncertainty. To further investigate the stability of these thermistors, they were later used in an experimental setup (at inlet, outlet and along the length of the channel) for the experiments at three different mass flow rates and at a constant chiller temperature. Data from these experiments (shown in Fig. 12 (a-c)) give further confirmation about their stability for the long run. Table: 2 contains information about the mean, maximum and minimum values of temperature probes along with type-A uncertainty data during calibration. In this table, T1, T2, T3 and T4 represent the temperature readings of four thermistors to be calibrated whereas PB_Cal1 and PB_Cal2 represent the temperature readings of AS115-4WIRE thermistor. For the measurement of uncertainty associated with temperature readings of these thermistors, the Type-A uncertainty analysis was carried out. Table: 2 contains the mean values along with uncertainties.

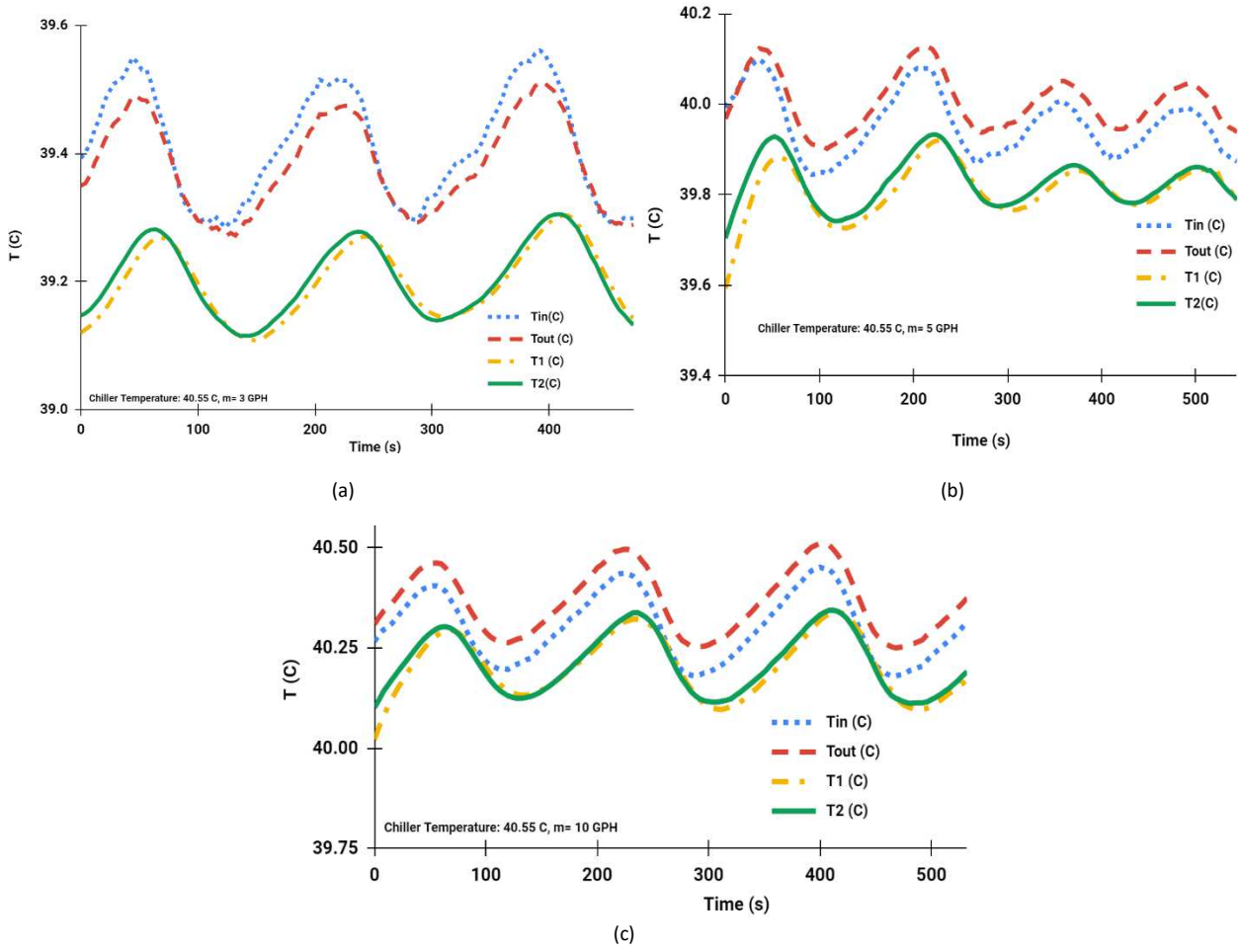
Table: 2 Data from calibration

Temperature (C)	T1	T2	T3	T4	PB_Cal1	PB_Cal2
T_{mean}	27.08	27.30	26.86	27.30	27.02	26.97
T_{Max}	27.13	27.40	26.90	27.32	27.05	26.98
T_{Min}	26.98	27.13	26.78	27.20	27.00	26.96
Uncertainty	0.053	0.057	0.052	0.053	-	-



(a) (b)

Fig. 11 (a-b) Temperature data at different chiller temperature during calibration



(a) (b)

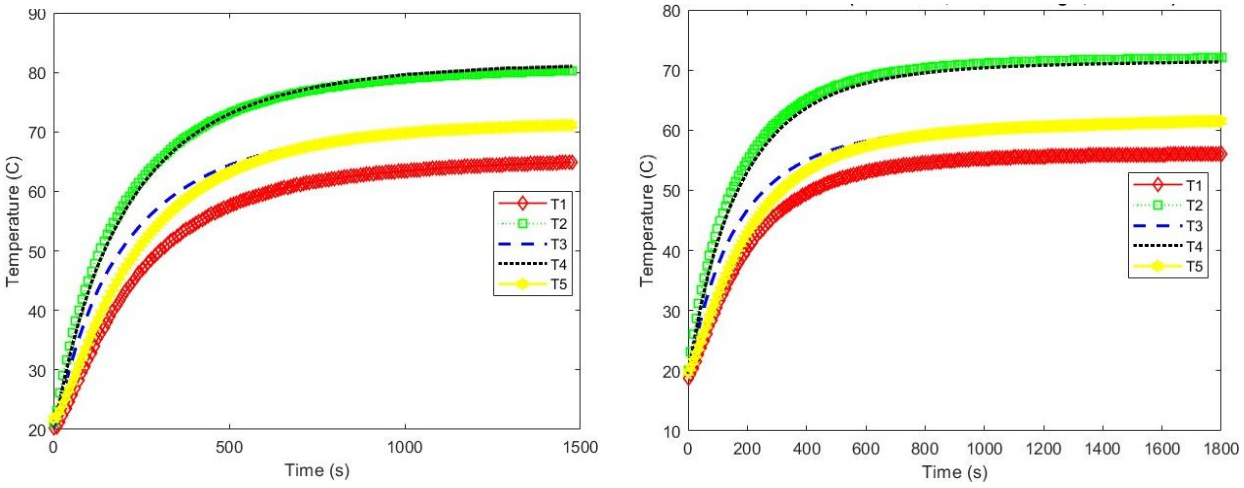
(c)

Fig. 12 (a-c) Probe temperatures at different chiller temperatures

8. Experimental investigation

For the experimental investigation of AM surfaces, the experimental set-up discussed in section-6 has been used for various flow conditions (from Re = 1000 to Re = 4000) and based on CFD simulations, 28.50 watts of heat was supplied through four E3D cylindrical heaters (diameter:6 mm, length: 20 mm, power: 12 W, voltage: 40 volt) and both current

(≈1.42 amp for each heater) and voltage (≈5 volt for each heater) were adjusted accordingly. All the experiments were run till the steady-state was achieved and mean temperature readings (sample size: for last 100 seconds) were used to calculate temperature at various locations. Fig. 13 shows the temperature vs time plot for two different Reynolds number with same heat input. In Fig. 13, T1, T2, T3, T4 and T5 are the temperature readings of thermistors (for five different holes) along the length of a parallel weld tracked (0° scan orientation) channel. To perform reproducibility tests, the entire setup was first dismantled and reassembled with existing SLA part and with new AM parts and with new heaters and thermistors of same specifications were used and later the type-A uncertainty analysis was carried out based on data collected from all the tests results. The uncertainty analysis is discussed in section-11.



(a) (b)

Fig. 13 (a) Temperature plot for Re = 2000, (b) Temperature plot for Re = 4000

9. CFD Modeling

CFD simulations were carried out for both smooth and rough cases and the entire system model of test setup was considered. For roughness modeling, in build sand-grain roughness model (represents, topography of surfaces with 90° build orientation) of Starccm+ were considered [8]. For CFD simulations, steady-state heat transfer and fluid-flow was considered. To resolve fluid-solid interface, conjugate heat-transfer model has also been considered [8-10]. External walls of test-setup were considered adiabatic because of high quality insulation used during experiments. For inlet and outlet of the channel, mass-flow inlet and pressure outlet boundaries were considered. To match the experimental conditions, the constant heat input was considered based on heat supply calculated during the experiments. To accurately resolve the roughness at fluid-solid interface and to treat the near wall heat transfer and fluid flow effectively, the k-ω RANS (SST) model has been used [8,10]. Simulations were done for the Reynolds numbers ranging from 1000 to 4000 to represent all critical flow conditions such as laminar, transient, and turbulent.

9.1 Equivalent sand-grain roughness model

The main goal of performing sand-grain CFD modeling is to correlate the CFD and experimental results of AM surface with 90° build orientation. As discussed in the introduction, to model surface roughness based on corrugated surface features, an in-built equivalent sand-grain roughness model (from Starccm+) has been used [8]. In this roughness model, sand grain size (k_s^+) can be expressed in a dimensionless form using dynamic (μ) and the friction velocity u* [17] as.

$$k_s^+ = \frac{K_s\, u^*}{\mu} \qquad (1)$$

$$u^* = \sqrt{\frac{\zeta_w}{\rho}} \qquad (2)$$

Here, K_s is roughness height calculated based on surface characterization discussed in section 5. ζ_w is a wall shear stress and ρ is a near wall fluid density

defined in the CFD model. Fig. 14 shows the analogy between the sand-grain roughness model and the roughness of AM surface with 90° build orientation. Though, it was assumed that the weld tracks are perfectly hemispherical and there no spatter and track variations were considered.

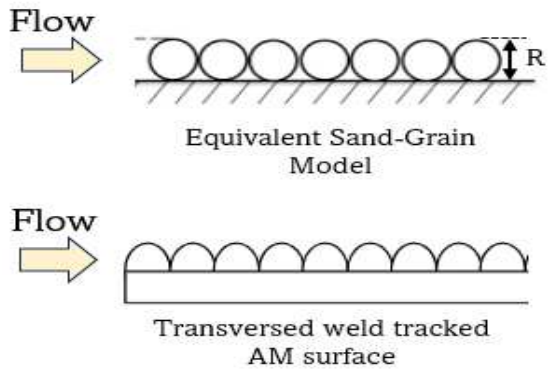


Fig. 14 Analogy between sand-grain surface and AM surface with 90° scan orientation.

9.2 Meshing and grid independence test

For the meshing, adoptive meshing technique was used and for incorporating the sand-grain roughness, one prismatic boundary layer was selected at solid-fluid interface and the layer thickness was kept higher than the roughness height. The base size of the meshing was 500 µm and the growth size of prismatic boundary layer cells was kept 15 percent of the base size. For the acceptable accuracy of the CFD results, grid independent tests were carried out and simulations were run from low number of cells to the optimized ones. For the optimization of number of cells, surface average temperature at outlet has been used as a criterion and plotted against the mesh size (shown in Fig. 15).

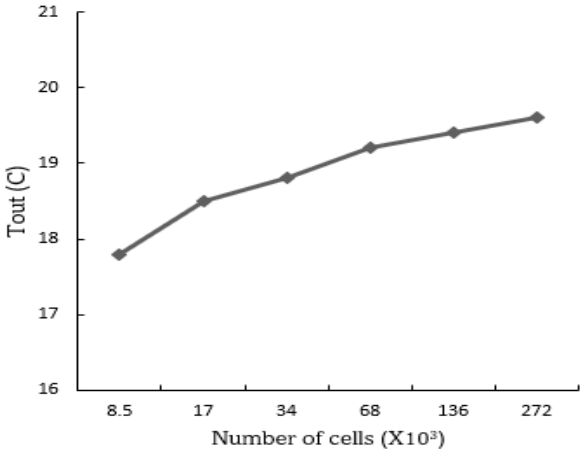


Fig. 15 Mesh independent analysis

10. Heat balance analysis

To ensure minimal heat leakage during experiments, high quality thermal insulation was used, and heat balance analysis was carried out to determine the heat loss to the environment. For heat balance, total heat input was calculated using Eq. 5 in which the mean values of voltage and current readings were used. To determine the heat carried away by water, Eq. 6 is used and when we subtract the heat carried away by water from the total heat input, we can determine the heat loss during each experiment.

$$q_{tot} = q_{fluid} + q_{loss} \quad (3)$$

$$q_{Loss} = q_{Tot} - q_{Fluid}\,, \quad (4)$$

$$q_{tot} = IV \quad , \quad (5)$$

$$q_{fluid} = mC_p\Delta T, \quad (6)$$

and

$$\Delta T = T_{out} - T_{in}. \quad (7)$$

Table: 3 Heat loss for various flow conditions

Mean Q (W)	Re ≈1000	Re ≈2000	Re ≈4000
Q_{Tot}	28.50	28.50	28.50
Q_{Fluid}	25.95	26.46	28.22
Q_{Loss}	2.60	2.03	0.94
% Q_{Loss}	8.90	7.12	3.30

11. Uncertainty analysis

The uncertainty analysis was carried out to evaluate the uncertainty associated with various parameters such as Nu, pressure drop (ΔP), heat input, friction factor and temperature at various locations. For determination of uncertainty, data from reproducibility tests were also considered and only Type-A uncertainty analysis [20-21] was carried out. During experiments, current, voltage, temperature and pressure drop were directly measured, and uncertainties associated with these quantities were determined based on standard deviation. However, Nu, f and heat input were determined using above

mentioned quantities therefore, law of propagation of error [20] was used to determine the uncertainty associated with them. Equations (8-10) are derived based on the law of propagation of error. However, the higher order terms were neglected due to the negligible contribution ($<10^{-4}$) in the uncertainty evaluation. Table: (4-6) contains results with their associated uncertainties.

$$U_q = q\sqrt{\left(\frac{U_I}{I}\right)^2 + \left(\frac{U_V}{V}\right)^2 + 2\frac{U_I.U_V}{I.V}}, \quad (8)$$

$$U_{Nu} = Nu\sqrt{\left(\frac{U_q}{q}\right)^2 + \left(\frac{U_{T_s}}{T_s}\right)^2 + \left(\frac{U_{T_m}}{T_m}\right)^2 + \left(\frac{U_{\overline{D}_H}}{\overline{D}_H}\right)^2 + 2\frac{U_q.U_{T_S}}{q.T_s}}, \quad (9)$$

and

$$U_f = f\sqrt{\left(\frac{U_{\Delta P}}{\Delta P}\right)^2 + \left(\frac{U_v}{v}\right)^2 + \left(\frac{U_{\overline{D}_H}}{\overline{D}_H}\right)^2 + 2\frac{U_{\Delta P}.U_v}{v.\Delta P}}. \quad (10)$$

Table: 4 Experimental values of parameters with uncertainty (Re ≈1K)

Parameters (Re ≈1K)	smooth	Paral (0°)	Angled (45°)	Trans (90°)
Nu	$22.8^{\pm 0.49}$	$22.7^{\pm 0.50}$	$22.6^{\pm 0.48}$	$23.8^{\pm 0.36}$
ΔP (Pa)	$360.3^{\pm 4.60}$	$384.5^{\pm 10.60}$	$388.3^{\pm 7.60}$	$370.3^{\pm 2.16}$

Table: 5 Experimental values of parameters with uncertainty (Re ≈ 2K)

Parameters (Re ≈ 2K)	smooth	Paral (0°)	Angled (45°)	Trans (90°)
Nu	$25.78^{\pm 0.57}$	$25.86^{\pm 0.57}$	$25.84^{\pm 0.56}$	$26.30^{\pm 0.40}$
ΔP (Pa)	$871.4^{\pm 16.00}$	$866.4^{\pm 14.04}$	$910.4^{\pm 15.00}$	$1034.2^{\pm 5.36}$

Table: 6 Experimental values of parameters with uncertainty (Re ≈ 4K)

Parameters (Re ≈ 4K)	smooth	Paral (0°)	Angled (45°)	Trans (90°)
Nu	$34.75^{\pm 0.78}$	$34.40^{\pm 0.79}$	$35.70^{\pm 0.80}$	$39.90^{\pm 0.67}$
ΔP (Pa)	$2506.6^{\pm 8.57}$	$2550.5^{\pm 11.57}$	$2650.6^{\pm 10.15}$	$3137.3^{\pm 8.9}$

11.1 Determination of temperature in CFD models

To accurately measure the temperature readings and to compare them with the CFD ones in a proper manner, a geometry [20] of the same size as the thermistor diameter were created in CFD models (shown in Fig. 16) and mean of surface average temperature was determined from CFD simulations. Also, to determine the temperature from the tip of the hole accurately (by avoiding contact between thermistor and hole wall), bigger holes (bigger than thermistor diameter) were made and the same is also considered for CFD models.

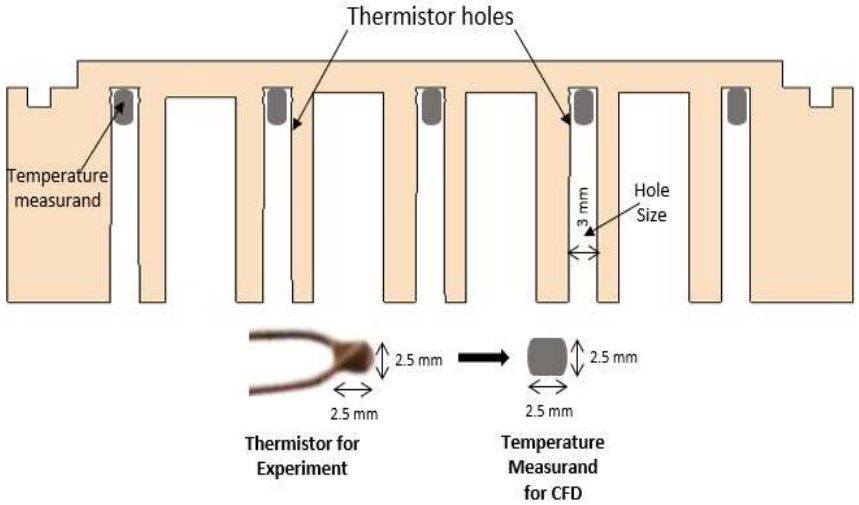


Fig. 16 Mid-plane view of CFD model with temperature measurand.

12. Results and discussion

For examining the thermal and fluid-flow characteristics of AM surfaces, results were analyzed in terms of Nusselt Number (Nu), pressure drop (ΔP), friction factor (f) and outlet temperature (T_{out}). Below equations are used for determining these parameters [22].

$$Nu = \frac{q''.\overline{D}_H}{K_f.(T_s - T_m)}, \qquad (11)$$

$$\Delta P = P_{in} - P_{out}, \qquad (12)$$

and

$$f = \frac{2.\Delta P.\overline{D}_H}{\rho.L.v^2}. \qquad (13)$$

Fig. 17 -20 show results in terms of ΔP, f, Nu and T_{out} for different AM surfaces at different Reynolds number whereas Fig. 21 shows the temperature profile along the length of the channels with different AM surfaces. From Fig. 17-20, it can be observed that the channel with transversed tracked surface (90° build orientation) gives highest amount of convective heat transfer (based on Nu) and so the pressure drop and friction factor. Both CFD and experimental results justify this statement. Whereas a channel with 45° oriented AM surface give optimal values of Nu and ΔP for different flow conditions. However, a channel with 0° build oriented surface has performed poorly for all flow conditions and sometimes poorer than the smooth one. Therefore, it is important to note that not all AM surfaces can provide a high rate of heat transfer and most importantly it depends on build-orientation and the flow conditions. From these results, it can also be observed that the surface with highest value of Nu (90° build orientation) also give higher pressure drop and thus it may require more pumping power depending on the scale of application. However, a surface with 45° build orientation provides optimal values both in terms of Nu and ΔP and can be used for most of the applications without compromising with the pumping power requirements.

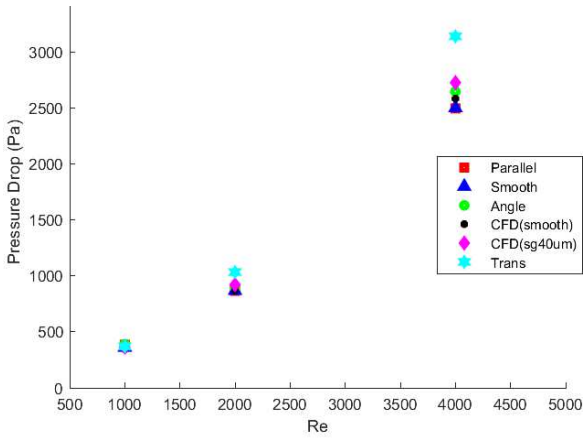


Fig. 17 Pressure drop for different Reynolds Number

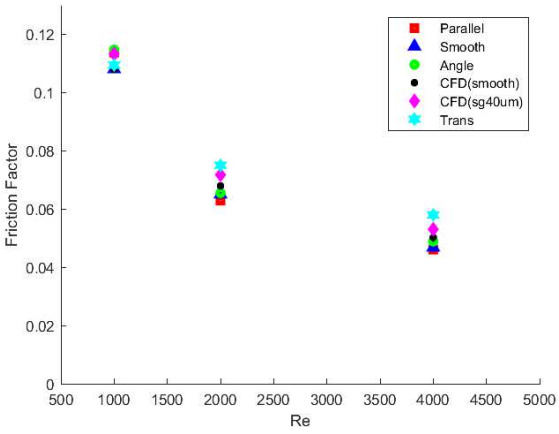


Fig. 18 Friction factor different Reynolds Number

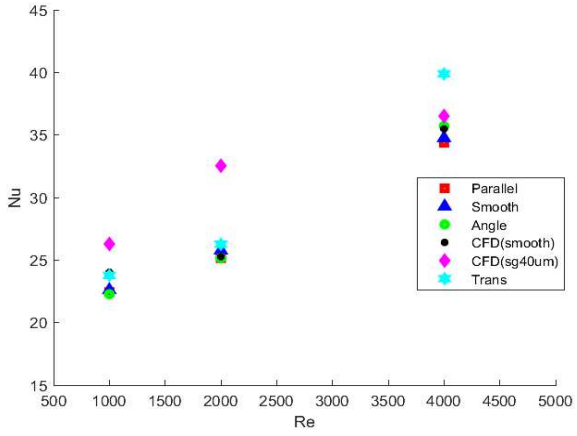


Fig. 19 Nusselt Number for different Reynolds Number

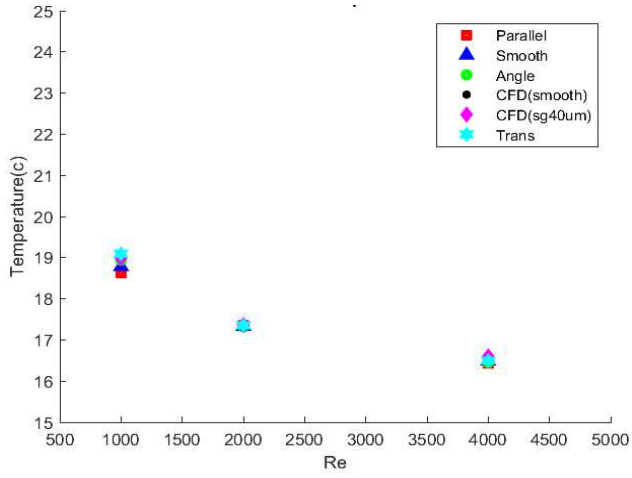
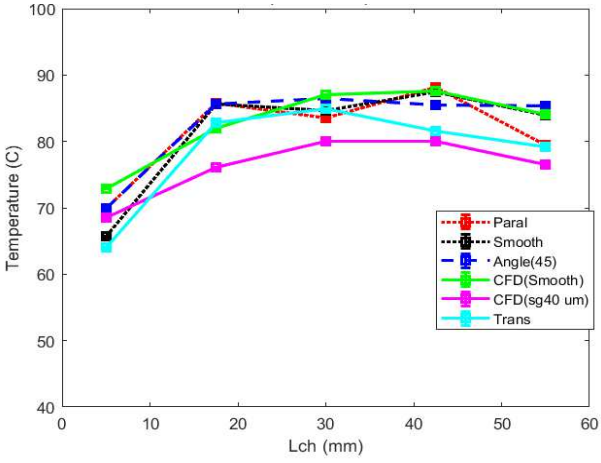
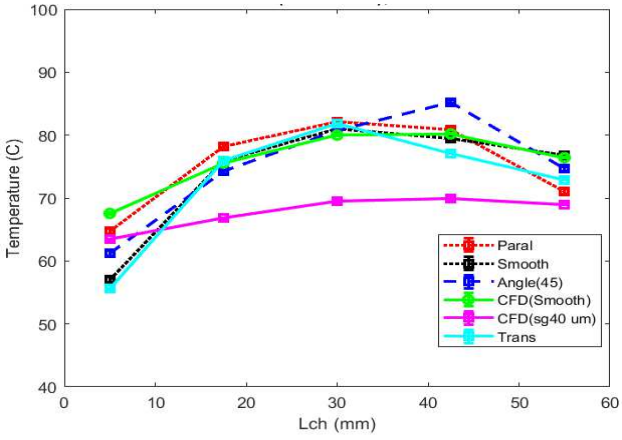


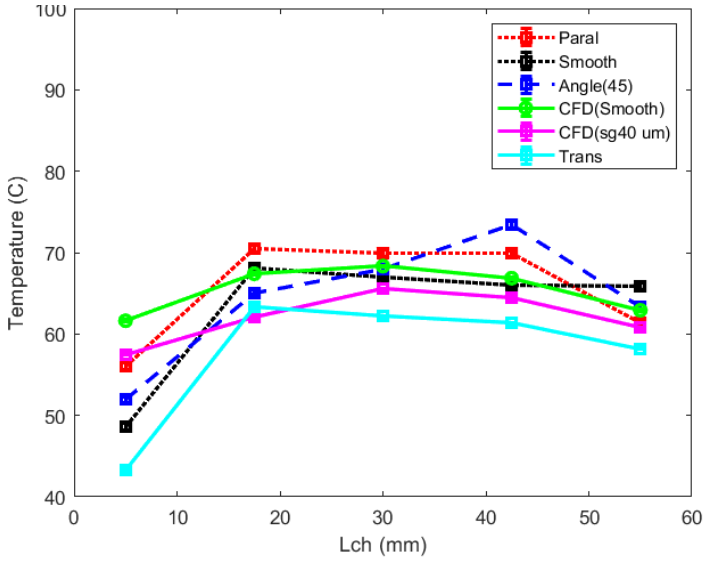
Fig. 20 Outlet temperature for different Reynolds Number



(a)



(b)



(c)

Fig. 21 (a) Temperature along channel length for Re =1000, (b) Temperature along channel length for Re =2000, (c) Temperature along channel length for Re =4000

13. Conclusion

To explore the relationship between the as-built surface finish of AM surfaces with different build-orientations and their resulting effects on heat transfer and fluid-flow, both CFD and experimental investigations were conducted. For CFD simulations, a sand-grain roughness model was adopted whereas for experiments, an innovative approach was used to design and develop an exchangeable experimental set-up and the investigations were carried out. For the reproducibility of the experimental results, experiments were carried out (three times) for each AM part at different time of intervals and based on experimental data, the Type-A uncertainty analysis was carried out. Based on nominal build conditions (laser power, scanning speed, layer thickness, powder and etc.), these results show that the track orientations of AM surfaces, and spatter deposits are the most dominating features of AM surfaces and the surface area impact on heat transfer is minimal for both laminar and turbulent flow conditions. Under turbulent flow conditions, transverse track alignment shows highest efficiency in terms of the Nu. However, when flow becomes laminar, most of these surfaces give similar Nu. The surface (90°) with highest Nu also performs poor in terms of ΔP whereas 45° oriented surface has lower Nu and ΔP compared to 90° tracked surface but performed better than 0° tracked surfaces and both CFD and experimental results justify these findings. Therefore, it is important to conclude that not all AM surfaces can provide a high rate of heat transfer and most importantly it all depends on scan-orientation and the flow conditions.

Funding Declaration

This work was funded by the Center for Precision Metrology (CPM) through an affiliate program at the University of North Carolina at Charlotte USA.

References

1. Mandloi, K., Evans, C., Fox, J., Cherukuri, H., Miller, J., Allen, A., ... & Donmez, A. (2021). Toward specification of complex additive manufactured metal surfaces for optimum heat transfer. Proc. Jt. Spec. Interest Group Meet. Euspen ASPE, St. Gallen, Switzerland.
2. Fox, J. C., Evans, C., & Mandloi, K. (2021). Characterization of laser powder bed fusion surfaces for heat transfer applications. CIRP Annals, 70(1), 467-470.
3. Delgado, J., Ciurana, J., & Rodríguez, C. A. (2012). Influence of process parameters on part quality and mechanical properties for

DMLS and SLM with iron-based materials. The International Journal of Advanced Manufacturing Technology, 60, 601-610.

4. Snyder, J. C., Stimpson, C. K., Thole, K. A., & Mongillo, D. (2016). Build direction effects on additively manufactured channels. Journal of Turbomachinery, 138(5), 051006.
5. Kandlikar, S. G., Schmitt, D., Carrano, A. L., & Taylor, J. B. (2005). Characterization of surface roughness effects on pressure drop in single-phase flow in minichannels. Physics of Fluids, 17(10).
6. Yuan, X., Tao, Z., Li, H., & Tian, Y. (2016). Experimental investigation of surface roughness effects on flow behavior and heat transfer characteristics for circular microchannels. Chinese Journal of Aeronautics, 29(6), 1575-1581.
7. Brezgin, D. V., Aronson, K. E., Mazzelli, F., & Milazzo, A. (2017). The surface roughness effect on the performance of supersonic ejectors. Thermophysics and Aeromechanics, 24, 553-561.
8. Mandloi, K., Allen, A., Cherukuri, H., Miller, J., Duttrer, B., & Raquet, J. (2023). CFD and experimental investigation of AM surfaces with different build orientations. Surface Topography: Metrology and Properties, 11(3), 034001.
9. Siemens Industries Digital Software. Simcenter STAR-CCM+, version 2020., Siemens 2021.
10. Kassab, A., Divo, E., Heidmann, J., Steinthorsson, E., & Rodriguez, F. (2003). BEM/FVM conjugate heat transfer analysis of a three-dimensional film cooled turbine blade. International journal of numerical methods for heat & fluid flow, 13(5), 581-610.
11. An introduction to computational fluid dynamics (The finite volume method) by H K Versteeg and W Malalasekera. ISBN: 978-0-13-127498-3 (2007).
12. Nikuradse J 1959 Laws of flow in rough pipes (translation of “Stromungsgetze in rauhen Rohren” 1933). NACA technical memorandum 1292.
13. Adams, T., Grant, C., & Watson, H. (2012). A simple algorithm to relate measured surface roughness to equivalent sand-grain roughness. International Journal of Mechanical Engineering and Mechatronics, 1(2), 66-71.
14. Kadivar, M., Tormey, D., & McGranaghan, G. (2021). A review on turbulent flow over rough surfaces: Fundamentals and theories. International Journal of Thermofluids, 10, 100077.
15. Bogard, D. G., Schmidt, D. L., & Tabbita, M. (1996). Characterization and laboratory simulation of turbine airfoil surface roughness and associated heat transfer (Vol. 78750, p. V004T09A044). American Society of Mechanical Engineers.
16. Forster VT. “Performance loss of modern steam-turbine plant due to surface roughness.” Proceedings of the Institution of Mechanical Engineers. (1966);181(1):391-422.
17. Musker, A. J. "Universal roughness functions for naturally occurring surfaces."

Transactions of the Canadian Society for Mechanical Engineering 6, no. 1 (1980): 1-6.

18. Nicolle, J., Hazel, B., & Gauthier, H. (2021, June). Experimental investigation to determine equivalent sand grain for very rough hydraulic surfaces. In IOP Conference Series: Earth and Environmental Science (Vol. 774, No. 1, p. 012129). IOP Publishing.
19. Tuomas Riipinen “Research report of heat treatment of AM alloys” VTT-R-00899-20.
20. Formlab material properties – high temp: Photopolymer Resin for Form 3D Printers https://formlabs-media.formlabs.com/datasheets/High_Temp_Technical.pdf (2016).
21. ISO and BIPM OIML. "Guide to the Expression of Uncertainty in Measurement." Geneva, Switzerland 122 : 16-17(1995).
22. Taylor B. N. Guidelines for Evaluating and Expressing the Uncertainty of NIST Measurement Results (rev. Diane Publishing; (2009).
23. Çengel Yunus A., Ghajar, A. J. Heat and Mass Transfer Fundamentals & Applications; McGraw-Hill Education (2015).